

Magnetic force and torque on particles subject to a magnetic field

F. Vogel, J-P. Pelteret*, S. Kaessmair and P. Steinmann

Chair of Applied Mechanics, Friedrich-Alexander Universität Erlangen-Nürnberg (FAU)

Egerlandstr. 5, 91058 Erlangen, Germany

Abstract

Materials that are sensitive to an applied magnetic field are of increased interest and use to industry and researchers. The realignment of magnetizable particles embedded within a substrate results in a deformation of the material and alteration of its intrinsic properties. An increased understanding of the influence of the particles under magnetic load is required to better predict the behaviour of the material. In this work, we examine two distinct approaches to determine the resulting magnetic force and torque generated within a general domain. The two methodologies are qualitatively and quantitatively compared, and we propose scenarios under which one is more suitable for use than the other. We also describe a method to compute the generated magnetic torque. These post-processing procedures utilize results derived from a magnetic scalar-potential formulation for the large deformation magneto-elastic problem. We demonstrate their application in several examples involving a single and two particle system embedded within a carrier matrix. It is shown that, given a chosen set of boundary conditions, the magnetic forces and torques acting on a particle are influenced by its shape, size and location within the carrier.

Keywords: Magnetoactive materials; Magnetostatics; Magnetoelasticity; Finite-Element Method

1. Introduction

Magneto-sensitive materials are of increasing prevalence in a variety of industries. This class of materials is commonly characterized by the presence of magnetizable particles in suspension in a non-magnetizable substrate. In the presence of a magnetic field, they change their material properties. Due to their ability to react to external magnetic

*Corresponding author: Jean-Paul Pelteret. Email: jean-paul.pelteret@ltm.uni-erlangen.de

stimulation, they find use in a broad range [20] of automotive [32], industrial [3] and robotics [27] applications, to name a few examples.

Optimizing the composition of these materials is challenging for numerous reasons. In the presence of a magnetic field, particles tend to form chain-like structures. The dynamic inter-particle interactions, as well as those between particles and their substrate (to which they may be strongly or weakly chemically bonded), are complex. Under magnetic loading, these interactions influence the particle migration, which may be temporary or permanent depending on the nature of the carrier. Particle agglomeration also affects the viscous or deformation properties of the bulk material. Direct numerical modelling of the moving particles is often difficult due to their size with respect to the simulated application. In such cases, material characterisation may be achieved with the use of representative volume elements (RVEs) or particle tracking methods, employed in the fields of solid and fluid mechanics, respectively.

Particles in fluidic suspension [19] have been investigated in detail. The carrier material is often assumed to be non-magnetizable and the particle assumed to demonstrate a magnetically linear behaviour. Typically in these works, discrete modelling techniques are commonly used, although dipole models [15, 18, 36], the fictitious domain method [1], boundary element method [31] and finite element method [16, 22] have also been applied. Numerical investigations on particles embedded in elastomers find application when introducing a RVE and applying different homogenization [13, 29] or averaging techniques [44]. The magnetostriction, as well as material strains and stresses, can be quantified using these approaches [2, 44]. The magnetic torque acting on an elliptical fibre in a composite has also been investigated by [13].

In the current work, we describe two methods for calculating the total magnetic force on a representative heterogeneous domain subject to a non-trivial magnetic field. What we call the weak method, allows for a rapid determination of the overall magnetic force, with the possibility to isolate single particle forces when the carrier matrix has a low relative permeability. The second method, so-called strong method, allows for a more detailed analysis of the forces generated within individual particles, as well as the computation of the magnetic torques. All calculations are embedded within a large deformation finite element framework that is capable of capturing the mechanical and magnetic non-linearities of the material. We choose the magnetic field as the independent variable of the problem. For doing so, a Legendre transformation of the energy function has to be performed to switch the dependency on the magnetic induction to a dependency on the magnetic field. For the numerical implementation, we correlate the magnetic field with the gradient of a magnetic scalar potential. However, we demonstrate that the description of the ponderomotive stress and force remain consistent regardless of the chosen independent variable. Numerous scenarios, in which a particle is embedded in an only slightly magnetizable medium, are evaluated and analysed using both methods thereby demonstrating the relative accuracy between the two. Our investigations are thus extensible to complex compound materials with inhomogeneous permeabilities and can serve as baseline to design suitable RVEs in a multi-scale simulations. They are not restricted to a non-magnetizable carrier as is often the case for applications involving magnetorheological elastomers. As different particle shapes and sizes were reported in [12] and [39], we perform parametric studies

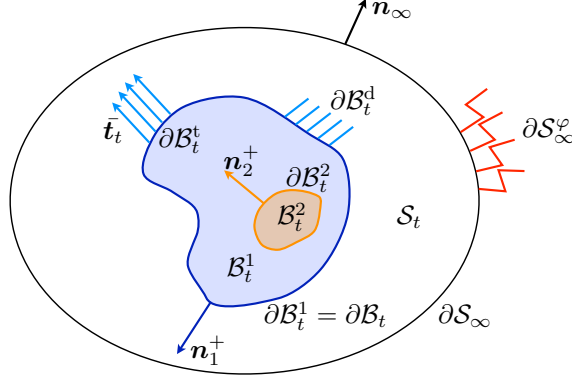


Figure 1: The continuum setting of a two material domain in the deformed configuration.

on the effect of particle size, shape and position in a non-uniform magnetic field. We conclude the examples by investigating the interaction of two particles immersed into a magnetic field.

This remainder of the manuscript is structured as follows: In section 2, we provide an overview of the equations relevant to the problem of magneto-elasticity. We describe the transformation of the total energy functional using a Legendre transformation in section 3. The description and implementation of two methods to calculate magnetic forces within the computational domain are presented in section 4. Several numerical examples are presented and discussed in section 5, which is followed by the conclusions.

2. General equations

With reference to fig. 1, we consider a deformed two-component body \mathcal{B}_t positioned within a second medium \mathcal{S}_t . Within the compound \mathcal{B}_t , two differently magnetizable materials occupy the regions \mathcal{B}_t^1 and \mathcal{B}_t^2 such that $\mathcal{B}_t = \mathcal{B}_t^1 \cup \mathcal{B}_t^2$. The interface between the two is denoted by $\partial\mathcal{B}_t^2$. \mathcal{S}_t represents the surrounding free space and the far-field boundary $\partial\mathcal{S}_\infty$ of \mathcal{S}_t is considered to be fixed in time and distant from \mathcal{B}_t . The complete boundary of \mathcal{S}_t can thus be described as $\partial\mathcal{S}_t = \partial\mathcal{S}_\infty \cup \partial\mathcal{B}_t$ where $\partial\mathcal{B}_t^1$ and $\partial\mathcal{B}_t$ coincide.

The boundary of the body is split such that mechanical Dirichlet boundary conditions are prescribed along $\partial\mathcal{B}_t^d$, whereas a Neumann condition in terms of prescribed mechanical tractions $\bar{\mathbf{t}}_t$ is given along $\partial\mathcal{B}_t^t$. The externally applied magnetic field is defined by a Dirichlet boundary condition along the boundary $\partial\mathcal{S}_\infty^\varphi$.

We define the spatial configuration \mathcal{B}_t such that $\mathbf{x} = \boldsymbol{\varphi}(\mathbf{X}, t)$ describes the non-linear mapping of points in the reference configuration \mathcal{B}_0 to this deformed configuration. The deformation gradient is then $\mathbf{F} := \nabla_{\mathbf{X}} \boldsymbol{\varphi}$ and the Jacobian $J = \det \mathbf{F}$ relates

the change in volumes between the two configurations.

Governing equations With respect to magnetism, we assume that the problem is static and there exist neither free surface nor free volume currents. The quasi-static Maxwell's equations for the spatial magnetic induction \mathbf{b} and the magnetic field \mathbf{h} read as

$$\nabla_{\mathbf{x}} \cdot \mathbf{b} = 0 \quad \text{and} \quad \nabla_{\mathbf{x}} \times \mathbf{h} = \mathbf{0} \quad \text{in} \quad \mathcal{B}_t \cup \mathcal{S}_t, \quad (2.1)$$

with the associated boundary and interface conditions given as

$$[[\mathbf{b}]] \cdot \mathbf{n}_i^+ = 0 \quad \text{on} \quad \partial \mathcal{B}_t^i, \quad (2.2)$$

$$[[\mathbf{h}]] \times \mathbf{n}_i^+ = \mathbf{0} \quad \text{on} \quad \partial \mathcal{B}_t^i, \quad \mathbf{h} \times \mathbf{n}_\infty = \mathbf{h}_\infty \times \mathbf{n}_\infty \quad \text{on} \quad \partial \mathcal{S}_\infty^\varphi, \quad (2.3)$$

with the jump of quantities defined as $[[\bullet]] := [\bullet]^{\text{outside}} - [\bullet]^{\text{inside}}$ and $i \in \{1, 2\}$. Equation (2.1)₂ is fulfilled exactly by deriving the magnetic field from a magnetic scalar potential

$$\mathbf{h} = -\nabla_{\mathbf{x}} \varphi \quad \text{in} \quad \mathcal{B}_t \cup \mathcal{S}_t. \quad (2.4)$$

The continuity and boundary conditions for the magnetic field translate then to conditions for the magnetic scalar potential

$$[[\varphi]] = 0 \quad \text{on} \quad \partial \mathcal{B}_t^i, \quad \varphi = \bar{\varphi}_\infty \quad \text{on} \quad \partial \mathcal{S}_\infty^\varphi. \quad (2.5)$$

Additionally, we can prescribe a Dirichlet boundary condition for the magnetic scalar potential along a subportion of $\partial \mathcal{B}_t$

$$\varphi = \bar{\varphi} \quad \text{on} \quad \partial \mathcal{B}_t^\varphi. \quad (2.6)$$

In free space, the relationship between the magnetic induction and the magnetic field is $\mathbf{b} = \mu_0 \mathbf{h}$ with the vacuum permeability μ_0 . In a general material, this relationship is no longer linear in \mathbf{h} , but is rather described by [21]

$$\mathbf{b} = \mu_0 [\mathbf{h} + \mathbf{m}] \quad \text{in} \quad \mathcal{B}_t, \quad (2.7)$$

where \mathbf{m} represents the magnetization of the material. With the help of the pull-back operations of the magnetic quantities

$$\mathbb{H} = \mathbf{h} \cdot \mathbf{F}, \quad \mathbb{B} = \mathbf{b} \cdot J \mathbf{F}^{-T}, \quad \mathbb{M} = \mathbf{m} \cdot \mathbf{F}, \quad (2.8)$$

it can be observed that eq. (2.7) translates in material configuration to

$$\mathbb{B} = \mu_0 J \mathbf{C}^{-1} \cdot [\mathbb{H} + \mathbb{M}] \quad \text{in} \quad \mathcal{B}_0. \quad (2.9)$$

As usual, $\mathbf{C} = \mathbf{F}^T \cdot \mathbf{F}$ denotes the right Cauchy-Green deformation tensor.

For the coupled magneto-mechanical problem, we neglect inertial forces and solve the balance of linear momentum [10, 11, 21, 34]

$$\nabla_{\mathbf{x}} \cdot \boldsymbol{\sigma} + \mathbf{b}_t^{\text{pon}} + \mathbf{b}_t = \nabla_{\mathbf{x}} \cdot \boldsymbol{\sigma}^{\text{tot}} + \mathbf{b}_t = \mathbf{0} \quad \text{in } \mathcal{B}_t, \quad (2.10)$$

where $\mathbf{b}_t^{\text{pon}}$ denotes the ponderomotive body force density and \mathbf{b}_t the mechanical body force density. Here, we define $\boldsymbol{\sigma}^{\text{tot}}$ as a symmetric Cauchy type total stress tensor [26, 34, 35, 40, 41] which includes the non-symmetric elastic stress $\boldsymbol{\sigma}$ as well as the additional ponderomotive contribution $\boldsymbol{\sigma}^{\text{pon}}$. In knowledge of the ponderomotive force term given in [4, 28], the ponderomotive stress is defined such that [7, 17, 21, 24, 25, 34]

$$\nabla_{\mathbf{x}} \cdot \boldsymbol{\sigma}^{\text{pon}} = \mathbf{b}_t^{\text{pon}} = \mathbf{m} \cdot \nabla_{\mathbf{x}} \mathbb{b} \quad \text{with} \quad \boldsymbol{\sigma}^{\text{pon}} = \frac{1}{2\mu_0} [\mathbb{b} \cdot \mathbb{b}] \mathbf{i} - [\mathbb{h} \cdot \mathbb{b}] \mathbf{i} + \mathbb{h} \otimes \mathbb{b}. \quad (2.11)$$

It is observed that, due to the magnetic contribution

$$\mathbf{g}_t^{\text{mag}} = \mathbf{m} \times \mathbb{b} \quad (2.12)$$

to the balance of angular momentum, the contribution from the elastic stresses $\boldsymbol{\sigma}$ is no longer symmetric. However, the total stress $\boldsymbol{\sigma}^{\text{tot}}$ is symmetric. A split of the ponderomotive stress in non-symmetric and symmetric parts [4–6, 8, 10, 17, 23, 37, 38], leads to the non-symmetric magnetization stress

$$\boldsymbol{\sigma}^{\text{mag}} = [\mathbf{m} \cdot \mathbb{b}] \mathbf{i} - \mathbf{m} \otimes \mathbb{b} \quad (2.13)$$

and the symmetric Maxwell stress

$$\boldsymbol{\sigma}^{\text{max}} = -\frac{1}{2\mu_0} [\mathbb{b} \cdot \mathbb{b}] \mathbf{i} + \frac{1}{\mu_0} \mathbb{b} \otimes \mathbb{b} =: -M_t \mathbf{i} + \frac{1}{\mu_0} \mathbb{b} \otimes \mathbb{b}. \quad (2.14)$$

with the spatial magnetic free field energy M_t . It should be mentioned that the ordinary Cauchy stress $\boldsymbol{\sigma}$, the magnetization \mathbf{m} and thus the ponderomotive stress $\boldsymbol{\sigma}^{\text{pon}}$ only exist inside matter. The Maxwell stress as well as the magnetic free field $\mathbb{h}^\mu := \mu_0^{-1} \mathbb{b}$ do not vanish outside matter, however, and both fulfill a divergence free condition.

A Piola transformation of $\boldsymbol{\sigma}^{\text{tot}}$ leads to a non-symmetric total Piola stress \mathbf{P}^{tot} in referential configuration together with the ponderomotive stresses

$$\mathbf{P}^{\text{tot}} = \boldsymbol{\sigma}^{\text{tot}} \cdot J \mathbf{F}^{-1}, \quad \mathbf{P}^{\text{mag}} = [\mathbb{M} \cdot \mathbb{B}] \mathbf{F}^{-T} - \mathbf{m} \otimes \mathbb{B}, \quad \mathbf{P}^{\text{max}} = -M_0 \mathbf{F}^{-T} + \mathbb{h}^\mu \otimes \mathbb{B}, \quad (2.15)$$

with the referential counterpart M_0 of M_t derived as

$$M_0(\mathbf{F}, \mathbb{B}) = \frac{1}{2\mu_0} J^{-1} \mathbf{C} : [\mathbb{B} \otimes \mathbb{B}]. \quad (2.16)$$

The jump and boundary conditions associated with the balance of linear momentum are

$$[[\boldsymbol{\varphi}]] = \mathbf{0} \quad \text{on } \partial \mathcal{B}_t^i, \quad [[\boldsymbol{\sigma}^{\text{tot}}]] \cdot \mathbf{n}_1^+ = -\bar{\mathbf{t}}_t \quad \text{on } \partial \mathcal{B}_t^t, \quad (2.17)$$

$$\boldsymbol{\varphi} = \bar{\boldsymbol{\varphi}} \quad \text{on } \partial \mathcal{B}_t^d, \quad \boldsymbol{\varphi}(\mathbf{X}) - \mathbf{X} = \mathbf{0} \quad \text{on } \partial \mathcal{S}_\infty. \quad (2.18)$$

Resultant ponderomotive force and torque acting on particle We consider the domain \mathcal{B}_t^2 as a particle suspended in a carrier matrix occupying the region \mathcal{B}_t^1 . We are interested in the resultant ponderomotive force and torque acting on the particle due to an externally applied magnetic field. According to [10, 14], the ponderomotive force acquires an additional surface contribution at the interface $\partial\mathcal{B}_t^2$ between particle and matrix. It holds that

$$\mathbf{f}^{\text{pon}} = \int_{\mathcal{B}_t^2} \nabla \mathbf{x} \cdot \boldsymbol{\sigma}^{\text{pon}} + \int_{\partial\mathcal{B}_t^2} \llbracket \boldsymbol{\sigma}^{\text{pon}} \rrbracket \cdot \mathbf{n}_2^+. \quad (2.19)$$

By exploiting eq. (2.11)₁ and introducing the definition of the ponderomotive tractions

$$\mathbf{t}_t^{\text{pon}} = \llbracket \boldsymbol{\sigma}^{\text{pon}} \rrbracket \cdot \mathbf{n}_i^+, \quad (2.20)$$

which can occur at all material discontinuities (both $\partial\mathcal{B}_t^1$ and $\partial\mathcal{B}_t^2$), we can rewrite the resultant ponderomotive force in the volume and along the interface as

$$\mathbf{f}^{\text{pon}} = \int_{\mathcal{B}_t^2} \mathbf{b}_t^{\text{pon}} + \int_{\partial\mathcal{B}_t^2} \mathbf{t}_t^{\text{pon}} =: \mathbf{f}_{\text{vol}}^{\text{pon}} + \mathbf{f}_{\text{int}}^{\text{pon}}. \quad (2.21)$$

Similarly, the magnetic moments can also be defined as

$$\mathbf{m}_{\text{pon}} = \int_{\mathcal{B}_t^2} [\mathbf{x} \times \mathbf{b}_t^{\text{pon}} + \mathbf{g}_t^{\text{mag}}] + \int_{\partial\mathcal{B}_t^2} [\mathbf{x} \times \mathbf{t}_t^{\text{pon}}] =: \mathbf{m}_{\text{pon}}^{\text{v}} + \mathbf{m}_{\text{pon}}^{\text{i}}. \quad (2.22)$$

Immediately from eqs. (2.21) and (2.22) it is observed that the ratio of ponderomotive forces and torques developed in the bulk and on the surface of solid bodies depend on several factors besides the constitution of the particle \mathcal{B}_t^2 itself. The size of the particle defines the surface area to volume ratio. Furthermore, the difference in relative magnetic permeability of adjacent materials affects the magnitude of the jump of the ponderomotive stress across the interface.

3. Constitutive relations and Legendre transformation of energy

To set up constitutive relations, it is assumed that the body \mathcal{B}_t is composed of magneto-sensitive material that is influenced by the magnetic field permeating it. We further assume the existence of a total energy per unit referential volume [8],

$$W_0(\mathbf{F}, \mathbb{B}) = \Psi_0(\mathbf{F}, \mathbb{B}) + M_0(\mathbf{F}, \mathbb{B}). \quad (3.1)$$

W_0 is additively decomposed into a contribution Ψ_0 , which accounts for the stored energy due to elastic deformation and magnetization, and the free field magnetic energy M_0 . The constitutive laws describing such a material are given as

$$\mathbf{P}^{\text{tot}} = \frac{\partial W_0}{\partial \mathbf{F}}, \quad \mathbb{H} = \frac{\partial W_0}{\partial \mathbb{B}}. \quad (3.2)$$

The corresponding decompositions into elastic and magnetic as well as Maxwell components can be derived as

$$\mathbf{P} + \mathbf{P}^{\text{mag}} = \frac{\partial \Psi_0}{\partial \mathbf{F}}, \quad \mathbf{P}^{\text{max}} = \frac{\partial M_0}{\partial \mathbf{F}}. \quad (3.3)$$

In an analogous manner, we can derive for the referential magnetic quantities

$$\mathbb{M} = -\frac{\partial \Psi_0}{\partial \mathbb{B}}, \quad \mathbb{H}^\mu := \frac{\partial M_0}{\partial \mathbb{B}} = \mu_0^{-1} J^{-1} \mathbf{C} \cdot \mathbb{B}, \quad (3.4)$$

where \mathbb{H}^μ denotes the referential magnetic free field. For the implicit definition eq. (3.4)₁ of the magnetization vector [42], we used the identity eq. (3.4)₂ in conjunction with eq. (2.9).

Since we assume no free currents and can therefore express the magnetic field in terms of the magnetic scalar potential φ (see eq. (2.4)), we perform a Legendre transformation on W_0 to switch the independent magnetic field variable from \mathbb{B} to \mathbb{H} . This approach is preferred due to its simplicity and straight-forward numerical implementation. The Legendre-transformation is defined as [5, 8]

$$W_0^*(\mathbf{F}, \mathbb{H}) = W_0(\mathbf{F}, \mathbb{B}(\mathbb{H})) - \mathbb{H} \cdot \mathbb{B}(\mathbb{H}) = \Psi_0^*(\mathbf{F}, \mathbb{H}) + M_0^*(\mathbf{F}, \mathbb{H}). \quad (3.5)$$

with M_0^* being the Legendre-transformation of M_0 in free space [41]

$$M_0^*(\mathbf{F}, \mathbb{H}) = -\frac{1}{2} \mu_0 J \mathbf{C}^{-1} : [\mathbb{H} \otimes \mathbb{H}]. \quad (3.6)$$

Exploiting the constitutive relation eq. (2.9) in eq. (3.5), one can straight-forwardly derive

$$\Psi_0^*(\mathbf{F}, \mathbb{H}) = \Psi_0(\mathbf{F}, \mathbb{B}(\mathbb{H})) + \frac{1}{2} \mu_0 J \mathbf{C}^{-1} : [\mathbb{M}(\mathbb{H}) \otimes \mathbb{M}(\mathbb{H})]. \quad (3.7)$$

The corresponding constitutive laws in the material setting are

$$\mathbf{P}^{\text{tot}} = \frac{\partial W_0^*}{\partial \mathbf{F}}, \quad \mathbb{B} = -\frac{\partial W_0^*}{\partial \mathbb{H}}. \quad (3.8)$$

This yields the corresponding decompositions of the stresses

$$\mathbf{P} + \mathbf{P}^{*\text{mag}} = \frac{\partial \Psi_0^*}{\partial \mathbf{F}}, \quad \mathbf{P}^{*\text{max}} = \frac{\partial M_0^*}{\partial \mathbf{F}}, \quad (3.9)$$

and the magnetic variables

$$\mu_0 J \mathbf{C}^{-1} \cdot \mathbb{M} = -\frac{\partial \Psi_0^*}{\partial \mathbb{H}}, \quad -\mu_0 J \mathbf{C}^{-1} \cdot \mathbb{H} = \frac{\partial M_0^*}{\partial \mathbb{H}}. \quad (3.10)$$

In analogy to eq. (3.4), we used for the implicit definition of the magnetization vector eq. (3.10)₁ the identity given in eq. (3.10)₂ together with the relation between the spatial magnetic fields eq. (2.9). Equation (3.10)₁ is also in line with eq. (3.7).

In the Legendre transformed total energy, the spatial description of the dependent variables, namely the Cauchy stress, magnetic induction and magnetization are

$$\boldsymbol{\sigma}^{\text{tot}} := J^{-1} \frac{\partial W_0^*}{\partial \mathbf{F}} \cdot \mathbf{F}^T, \quad \mathbb{b} = -J^{-1} \frac{\partial W_0^*}{\partial \mathbb{H}} \cdot \mathbf{F}^T, \quad \mathbb{m} = -\mu_0^{-1} J^{-1} \mathbf{F} \cdot \frac{\partial \Psi_0^*}{\partial \mathbb{H}}. \quad (3.11)$$

Correspondingly, the Maxwell stress now takes the format

$$\boldsymbol{\sigma}^{*\text{max}} = -\frac{1}{2} \mu_0 [\mathbb{h} \cdot \mathbb{h}] \mathbf{i} + \mu_0 \mathbb{h} \otimes \mathbb{h} = M_t^* \mathbf{i} + \mu_0 \mathbb{h} \otimes \mathbb{h}, \quad (3.12)$$

while the magnetization stress can be derived as

$$\boldsymbol{\sigma}^{*\text{mag}} = \frac{1}{2} \mu_0 [\mathbb{m} \cdot \mathbb{m}] \mathbf{i} + \mu_0 \mathbb{h} \otimes \mathbb{m}. \quad (3.13)$$

For a detailed derivation of the magnetization stresses $\boldsymbol{\sigma}^{*\text{mag}}$, we refer the reader to appendix A. Summation of $\boldsymbol{\sigma}^{*\text{max}}$ and $\boldsymbol{\sigma}^{*\text{mag}}$ leads to a ponderomotive stress $\boldsymbol{\sigma}^{*\text{pon}}$, which takes the identical form to that previously described in eq. (2.11)₂.

$$\boldsymbol{\sigma}^{*\text{pon}} = \boldsymbol{\sigma}^{*\text{max}} + \boldsymbol{\sigma}^{*\text{mag}} = \boldsymbol{\sigma}^{\text{pon}} \quad (3.14)$$

Therefore, regardless of the choice of the independent variable, the decomposition into Maxwell and magnetic stress as in eqs. (3.12) and (3.13) remains consistent with the definition of the ponderomotive body force as in eq. (2.11)₁. Furthermore, it can be demonstrated that a re-parameterisation of the total energy function in terms of the spatial magnetic quantities leads to constitutive laws in accordance with those presented in [34].

4. Finite element approximation

4.1. Solution of the weak form

From the balance of forces and the Maxwell equation, the variation of the total potential energy

$$\begin{aligned} \delta \Pi = & \int_{\mathcal{B}_t} \boldsymbol{\sigma}^{\text{tot}} : \nabla_{\mathbf{x}} \delta \boldsymbol{\varphi} + \mathbb{b} \cdot \nabla_{\mathbf{x}} \delta \varphi + \int_{\mathcal{S}_t} \boldsymbol{\sigma}^{*\text{max}} : \nabla_{\mathbf{x}} \delta \boldsymbol{\varphi} + \mathbb{b} \cdot \nabla_{\mathbf{x}} \delta \varphi \\ & - \int_{\mathcal{B}_t} \mathbf{b}_t \cdot \delta \boldsymbol{\varphi} - \int_{\partial \mathcal{B}_t} \bar{\mathbf{t}}_t \cdot \delta \boldsymbol{\varphi} \end{aligned} \quad (4.1)$$

is equal to zero when the system is in equilibrium. As is discussed in [43], the finite element method can be used to solve for the stationary point of the total potential energy functional given in eq. (4.1).

This coupled problem has been implemented using the following Galerkin finite element approximations

$$\varphi \approx \sum_I \varphi_I N_I, \quad \varphi \approx \sum_I \varphi_I N_I \quad (4.2)$$

$$\nabla_{\mathbf{x}} \varphi \approx \sum_I \varphi_I \otimes \nabla_{\mathbf{x}} N_I, \quad \nabla_{\mathbf{x}} \varphi \approx \sum_I \varphi_I \nabla_{\mathbf{x}} N_I, \quad (4.3)$$

where N_I represent the shape functions and $\nabla_{\mathbf{x}} N_I$ their respective spatial gradients. For both the deformation and magnetic scalar potential, the finite element approximation results in a continuous solution field but piecewise discontinuous solution gradients. Equation (2.5)₁ is strongly fulfilled through the use of node-based finite elements. The condition stated in eq. (2.2)₁, comparable to the traction-free condition for the mechanical stress, is only fulfilled weakly as the magnetic induction is the dependent variable.

4.2. Ponderomotive force and torque acting on a particle

Subsequent to the computation of the equilibrium of the magneto-mechanical problem, the post-processing steps to compute the resultant ponderomotive force and torque can be performed. Two methods are provided below, which can be used to compute the ponderomotive force and torque acting on an arbitrary subdomain $\mathcal{B}_t^2 \subset \mathcal{B}_t$ such as that occupied by a particle.

4.2.1. Computations derived from the strong form (SF) of balance of momentum

In the first method, which we call the strong form (SF), we pursue a strong evaluation of the ponderomotive force and torque as given in eqs. (2.21) and (2.22). Two features require special attention:

Firstly, the calculation of the gradient of the magnetic induction necessitates a smoothed magnetic induction field because the gradient needs to be evaluable also within a low-order finite element approach. A reformulation of $\nabla_{\mathbf{x}} \mathbb{b}$ in terms of the magnetic field \mathbb{h} via the constitutive law would feature second order derivatives of the magnetic scalar potential. These derivatives vanish, however, when linear shape functions are utilized for the magnetic scalar potential. Thus, a reformulation is not the favored approach and the smoothing is inevitable.

Secondly, in order to attain a jump in the ponderomotive stress across a material interface, it is necessary to allow for discontinuous magnetic fields across surface discontinuities. Thus, the smoothing may not annihilate the discontinuity property of the magnetic induction at an interface but must preserve it.

To account for both difficulties, the magnetic induction is initially computed at each quadrature point from the constitutive law (3.11)₂ of the corresponding material. It is subsequently projected to the nodes using a \mathcal{L}^2 smoothing procedure [33]. This procedure is performed individually for each material subdomain \mathcal{B}_t^i , thus generating

double values along all material discontinuities. This caters for the reasonable expectation that the magnetic field quantities are smooth on a per-material basis, but possibly discontinuous across material interfaces.

The smoothed magnetic induction $\tilde{\mathbb{b}}^i(\mathbf{x})$ within \mathcal{B}_t^i can be computed by solving the linear problem

$$\mathbf{M}_{IJ}^i \tilde{\mathbb{b}}_J^i = \mathbb{b}_I, \quad (\text{no summation over } i) \quad (4.4)$$

where $\tilde{\mathbb{b}}_J^i$ represent the nodal values of the smoothed magnetic induction. The contributions for the consistent mass matrix and right-hand side are

$$\begin{aligned} \mathbf{M}_{IJ}^i &= \sum_{h \in \mathcal{B}_t^{i,h}} \sum_q N_I(\mathbf{x}_q^h) N_J(\mathbf{x}_q^h) w_q^h \quad \text{and} \\ \mathbb{b}_I &= \sum_{h \in \mathcal{B}_t^{i,h}} \sum_q \mathbb{b}(\mathbf{x}_q^h) N_I(\mathbf{x}_q^h) w_q^h \end{aligned} \quad (4.5)$$

with h representing an element in the discretized domain $\mathcal{B}_t^{i,h}$, q the local numbering of the quadrature points, \mathbf{x}_q^h the real position of each quadrature point and w_q^h a weighting factor belonging to the numerical integration. The smoothed value and approximated gradient of the magnetic induction at any position within \mathcal{B}_t^i are therefore given by

$$\tilde{\mathbb{b}}^i(\mathbf{x}) \approx \sum_J \tilde{\mathbb{b}}_J^i N_J(\mathbf{x}) \quad \text{and} \quad \nabla_{\mathbf{x}} \tilde{\mathbb{b}}(\mathbf{x}) \approx \sum_J \tilde{\mathbb{b}}_J^i \otimes \nabla_{\mathbf{x}} N_J(\mathbf{x}). \quad (4.6)$$

The same procedure is applied to compute the subdomain-restricted smoothed fields of the magnetization and magnetic field. We indicate the use of subdomain smoothing prior to the evaluation of eqs. (2.21) and (2.22) by the suffix S in subsequent text, tables and result figures.

Alternatively to the exclusive usage of smoothed fields, also a non-smoothing technique is performed, which we denote subsequently by NS . In this approach, only the magnetic induction is \mathcal{L}^2 projected because of its gradient calculation, but the values of the magnetization are stored for each quadrature point (qp) during the equilibrium loop when solving for the stationary point of (4.1). These values are reused to evaluate the volume integrals in eqs. (2.21) and (2.22). For the computation of the interface terms, the values of \mathbb{b} and \mathbb{h} are first extrapolated elementwise from the quadrature points to the nodes of each element, and then interpolated to the quadrature points on the element's face. A comparison of the variables used for smoothed and non-smoothed technique can found in table 1.

4.2.2. Computations derived from a variational (weak) form (WF) of the balance of momentum

For the derivation of the second approach to calculate the ponderomotive force, we consider a cut-out as computational domain \mathcal{D}_t , which is depicted in fig. 2a. \mathcal{D}_t represents a particle surrounded by magnetizable material. As is detailed in appendix B,

Table 1: Clarification of smoothed and non-smoothed technique for the strong form calculation

strong form (SF)	volume		interface	
	m	$\nabla_{\mathbf{x}} \mathbf{b}$	h	\mathbf{b}
smoothed (S)	\mathcal{L}^2 projected	\mathcal{L}^2 projected	\mathcal{L}^2 projected	\mathcal{L}^2 projected
non-smoothed (NS)	stored for each qp	\mathcal{L}^2 projected	extrapolated	extrapolated

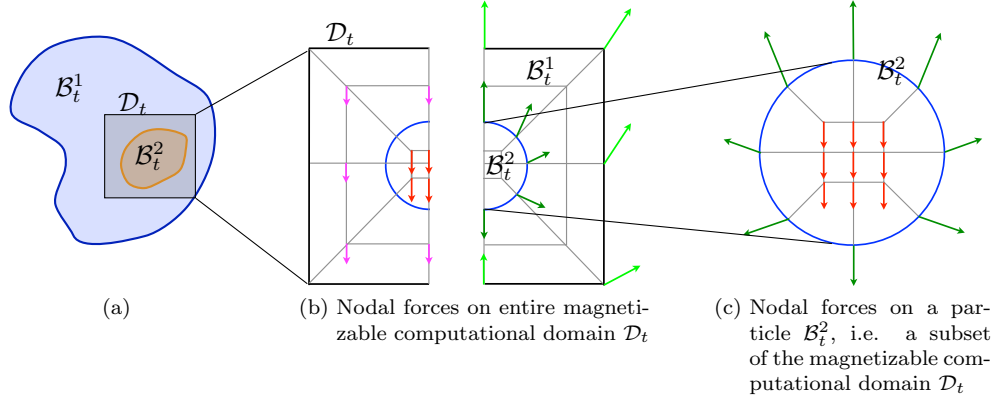


Figure 2: Nodal forces computed using the weak formulation of the ponderomotive force.

an alternate description of the total ponderomotive force acting on the domain can be developed from the weak form of the balance of momentum. We denote this approach by the abbreviation (WF). The result is a global node vector of ponderomotive forces computed by

$$\begin{aligned}
 \mathbf{f}_I^{\text{pon}} &= \int_{\mathcal{D}_t} N_I \mathbf{b}_t^{\text{pon}} + \int_{\partial \mathcal{B}_t^2} N_I \mathbf{t}_t^{\text{pon}} \\
 &= \int_{\partial \mathcal{D}_t} N_I [\boldsymbol{\sigma}^{\text{pon}} \cdot \mathbf{n}_{\partial \mathcal{D}_t}] - \int_{\mathcal{D}_t} \mathbf{B}_I \cdot \boldsymbol{\sigma}^{\text{pon}}.
 \end{aligned} \tag{4.7}$$

The resultant ponderomotive force on the computational domain \mathcal{D}_t is simply

$$\mathbf{f}_{\mathcal{D}_t}^{\text{pon}} = \sum_{I \in \mathcal{D}_t} \mathbf{f}_I^{\text{pon}}. \tag{4.8}$$

Compared to the method described in section 4.2.1, the computation in eq. (4.7) is easy to implement and computationally inexpensive to perform. However, as the

Table 2: Clarification of smoothed and non-smoothed technique for the weak form calculation

weak form (WF)	volume σ^{pon}	boundary σ^{pon}
smoothed (S)	\mathcal{L}^2 projected	\mathcal{L}^2 projected
non-smoothed (NS)	stored for each qp	extrapolated

sketch in fig. 2b shall illustrate, the result of eq. (4.7) are nodal force vectors distributed over the whole computational domain with extraordinary strong forces at material interfaces and the outer boundary. The outcome of eq. (4.8) is the resultant ponderomotive force acting on all magnetizable materials in the domain. That is to say, one cannot immediately distinguish between forces acting on the matrix or on individual particles. Especially along interfaces, where the magnitude of the nodal forces is much higher than compared to the volume, the assignment of nodal forces to the adjoining subdomains is ambiguous. However, if the physical nature of the media is such that the difference in magnetic permeabilities between the materials is large, then the ponderomotive forces computed at each interface node will be dominated by the greater relative permeability. Therefore, we count them among the higher permeable material. A zoom into the particle as in fig. 2c, illustrates that the total ponderomotive force in the subdomain \mathcal{B}_t^2 is then

$$\mathbf{f}_{\mathcal{B}_t^2}^{\text{pon}} = \sum_{I \in \mathcal{B}_t^2} \mathbf{f}_I^{\text{pon}}. \quad (4.9)$$

Due to the nature of this procedure, the boundary integral in eq. (4.7) can be ignored if the particle does not extend to the edge of the computational domain, that is if $\partial\mathcal{D}_t \cap \partial\mathcal{B}_t^2 = \emptyset$. In such a case, the boundary term will not contribute to any relevant entries in $\mathbf{f}_I^{\text{pon}}$.

As before in the strong form calculation, we distinguish also for the weak form between a smoothing and a non-smoothing technique. This reduces in the case of the weak form calculation to the \mathcal{L}^2 projection of the ponderomotive stress tensor σ^{pon} . A clarification of the variables used for smoothed and non-smoothed computation can found in table 2.

5. Numerical examples

For our numerical examples, we consider as basic geometry a cut-out \mathcal{D}_t of the body \mathcal{B}_t as already motivated in fig. 2a. Figure 3 provides a generic description of the particle problem which will be considered in various scenarios beginning in section 5.2. A single particle \mathcal{B}_t^2 is embedded in a surrounding matrix \mathcal{B}_t^1 of side-length l and thickness t . The blue cross indicates the origin of the domain, while the red cross marks the centroid of the particle. The elliptical particle, with major and minor axis

lengths a and b , is offset by a value o from the origin and rotated through an angle ϕ about the z -axis. For the purpose of simplification, we assume that the influence of the free space can be ignored and that the magnetic scalar potential is prescribed at the surface $\partial\mathcal{D}_t$. The boundary $\partial\mathcal{D}_t$ is split into four subregions $\partial\mathcal{D}_t^1$ through $\partial\mathcal{D}_t^4$ to prescribe different values of φ .

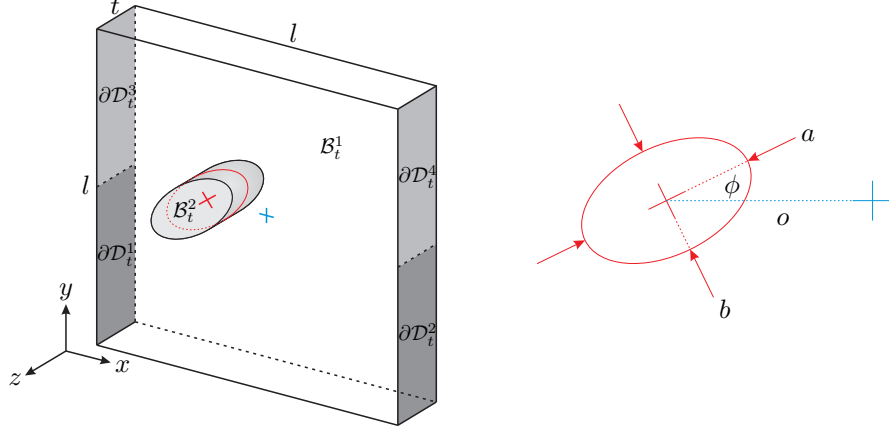


Figure 3: Diagrammatic sketch of a generic particle problem.

The magnetizable particle is composed completely of iron with a relative permeability of $\mu_p = 5000$, while the surrounding matrix is only slightly permeable with a relative permeability of $\mu_m = 10$. The constitutive law utilized for all materials describing a linear magnetic material behaviour is

$$\Psi_0^*(\mathbf{F}, \mathbb{H}) := -\frac{1}{2}\mu_0 [\mu_r - 1] \mathbf{J} \mathbf{C}^{-1} : [\mathbb{H} \otimes \mathbb{H}], \quad (5.1)$$

where μ_r is a general place holder for the relative permeabilities and must be replaced by either μ_p or μ_m .

Within the problems demonstrated in sections 5.1 to 5.3, the displacement degrees-of-freedom are fixed at zero value in order to concentrate on the magnetic effects. This represents the instantaneous result at the initial time of a dynamic simulation in the case of a matrix, or that at any time if the surrounding medium \mathcal{B}_t^1 represents a fluid. The constraint on the deformation is dropped in section 5.4. Linear hexahedral finite elements have been utilized for the magnetic potential field in the computational simulation of each scenario.

5.1. Validation of the volume force and torque computation for a magnetizable cube

In order to validate the implementation, we compute the volume force and torque on a cube for a given magnetic scalar potential and compare the numerical calculation in

the strong and the weak form with the analytical solution. We consider a cube with edge length $t = l = 2mm$. The cube is centered at the origin and completely composed of iron with $\mu_r = 5000$. The potential field, defined in terms of the spatial coordinates $\mathbf{x} = (x, y, z)$ in mm

$$\varphi(\mathbf{x}) = x^2 [x + y + 1],$$

is prescribed for both boundary and volume degrees of freedom. The resulting magnetic field is shown in fig. 4a.

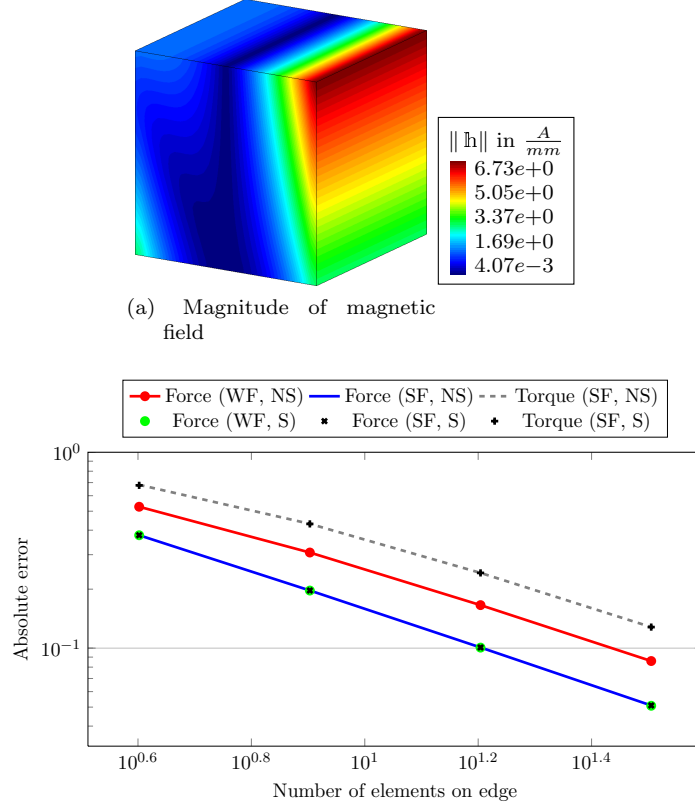


Figure 4: Numerical validation of ponderomotive volume force and torque for a magnetizable cube subject to a prescribed asymmetric potential

The resulting magnetic force is comprised only of volumetric force terms as a single material extends throughout the computational domain without any discontinuities. Therefore, the ponderomotive force and torque does not acquire any additional surface contributions. The analytical solution to the resulting ponderomotive body force,

determined directly from the prescribed potential field in conjunction with the linear magnetic material relationships, is calculated to be

$$\int_{\mathcal{D}_t} \mathbf{b}_t^{\text{pon}} = \mu_0 \mu_r [\mu_r - 1] \frac{16}{3} \begin{bmatrix} 9 \\ 2 \\ 0 \end{bmatrix}, \quad (5.2)$$

while the resulting torque developed in the body is

$$\int_{\mathcal{D}_t} \mathbf{x} \times \mathbf{b}_t^{\text{pon}} = \mu_0 \mu_r [\mu_r - 1] \frac{32}{5} \begin{bmatrix} 0 \\ 0 \\ -1 \end{bmatrix}. \quad (5.3)$$

It should be mentioned here, that the contribution of the magnetic couple $\mathbf{g}_t^{\text{mag}}$ to the ponderomotive torque is zero for linear magnetic materials, since the magnetization and the magnetic induction are then in parallel.

Figure 4b illustrates the convergence characteristics of the force and torque computed by the finite element method. As expected, with increasing mesh-refinement, the solution determined by all methodologies converge linearly towards the analytical solutions given in eqs. (5.2) and (5.3). However, it was observed that using the weak approach in conjunction with non-smoothed magnetic quantities produced inferior results in comparison to the other methods that produced identical results. The superiority of the smoothed values is expected as smoothing procedures lead to better approximations, which have also been used as reference solutions for error estimates [30, 45]. It is also interesting to note that the use of linear elements appears to, in the limit, have no impact on the quality of the solution. The magnetic torque computed using the strong formulation displayed similar convergence characteristics, with acceptable results attained at high grid resolution.

5.2. Validation of the surface traction and torque computation for a single cylindrical particle centered in a symmetric magnetic field

By considering the effect of an externally generated symmetric magnetic field on an individual cylindrical particle in a matrix, a validation of the interface force and torque computations in the strong form (SF) has been achieved. The rigid particle of diameter $a = b = 1\text{mm}$ is centered ($o = 0\text{mm}$) within a rectangular box with side length $l = 10\text{mm}$ ¹ (See fig. 3). For the sake of simplicity, in all cases the geometry has a 2.5d representation² with the domain extending $t = 0.4\text{mm}$ into the third dimension. A constant potential of $\pm 1000\text{A}$ prescribed on two opposing boundary surfaces $\partial\mathcal{D}_t^1 \cup \partial\mathcal{D}_t^3$ and $\partial\mathcal{D}_t^2 \cup \partial\mathcal{D}_t^4$ develops the symmetric potential field shown in fig. 5a.

¹ The boundary must be sufficiently distant from the particle for the analytical solution, which assumes an infinite domain, to remain valid.

² In these scenarios, it is more precise to say that the particles represent infinitely long fibres of specified cross-section embedded within a domain of infinite depth.

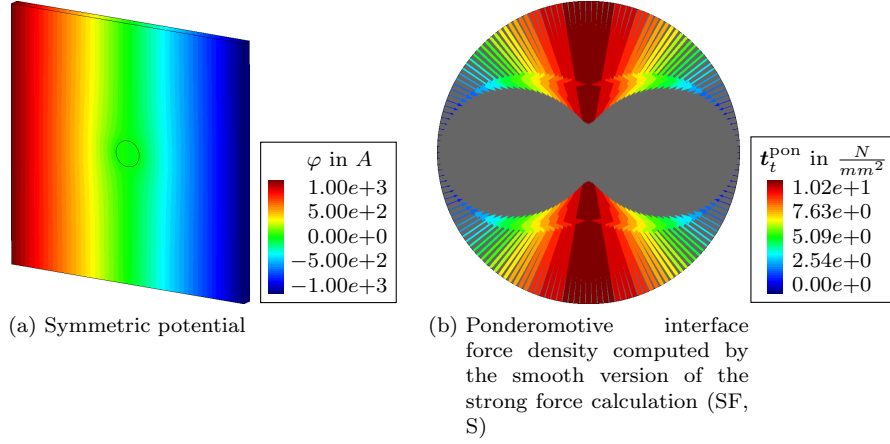


Figure 5: Single cylindrical particle (diameter 1mm) in symmetric magnetic field generated by a scalar potential prescribed along the whole vertical boundary

Due to the symmetric nature of the magnetic field, no resultant ponderomotive force or torque is produced. However, the presence of the particle results in a spatially non-homogeneous magnetic field and therefore non-trivial volume force densities and tractions arise. Development of the analytical solution at the material interface assumes that the matrix domain extends infinitely in all directions. Using potential theory [9], it can be demonstrated that the magnetic field at the interface from the view-point of the particle is

$$\mathbb{h}_p = |\mathbb{h}_\infty| \begin{bmatrix} B \\ 0 \\ 0 \end{bmatrix}, \quad B = \frac{2\mu_m}{\mu_p + \mu_m} \quad (5.4)$$

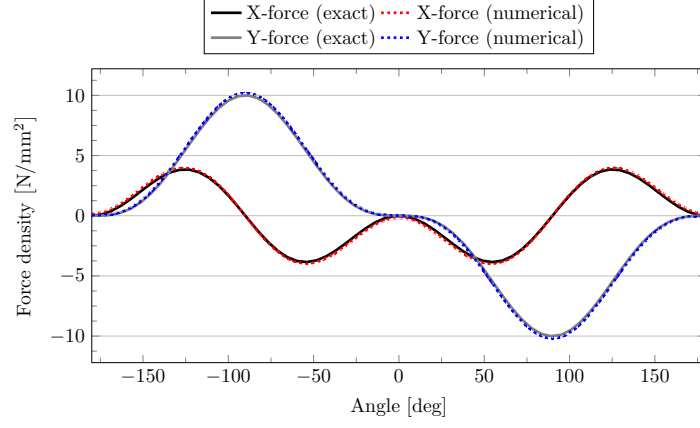
while from the matrix side, the magnetic field is

$$\mathbb{h}_m = |\mathbb{h}_\infty| \begin{bmatrix} 1 + C \cos(2\phi) \\ C \sin(2\phi) \\ 0 \end{bmatrix}, \quad C = \frac{\mu_p - \mu_m}{\mu_p + \mu_m} \quad (5.5)$$

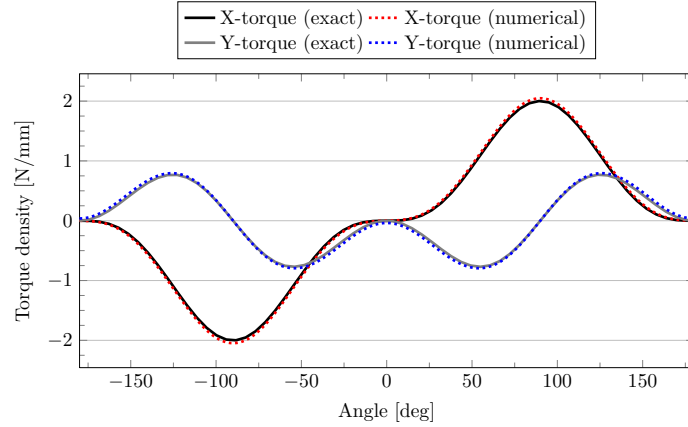
where the azimuthal angle ϕ provides the position of measurement along the circumference of the interface with respect to the direction of the far-field magnetic field. The magnetic induction and resulting force and torque can be computed after the application of the constitutive law.

Shown in fig. 5b is the point-wise representation of the ponderomotive traction developed at the interface between the particle and matrix. The volumetric force developed within the particle is negligible. However, the interface forces are compressive in the direction perpendicular to the applied external magnetic field and, if left unconstrained, would result in a deformation of the particle.

Components of the interface force and the in- and out-of-plane torque densities, measured radially, are compared in fig. 6 to the analytical solution. It is demonstrated



(a) Comparison of analytical and numerical strong form solution of ponderomotive tractions along mid-circumference of interface



(b) Comparison of analytical and numerical strong form solution of ponderomotive torque densities along upper (+z) circumference of interface

Figure 6: Numerical validation of the smooth form of the strong force computation (SF, S) of ponderomotive interface force and torque for a single particle (diameter 1mm) centered in a symmetric magnetic field

that the numerical values fit extremely well to those determined analytically. The symmetries of the resulting data indicate that, as expected, no resultant force or torque is induced in the particle.

5.3. Single cylindrical particle in asymmetric magnetic field

The scenario described in section 5.2 was modified such that the Dirichlet constraints on $\partial\mathcal{D}_t^3$ and $\partial\mathcal{D}_t^4$ were removed. When the particle remains centered within the matrix, the developed potential field illustrated in fig. 7a results in the magnetic field presented in fig. 7b. Herein, the influence of the particle on the asymmetric magnetic field can be clearly observed, as well as the presence of a high field gradient at the intersection from $\partial\mathcal{D}_t^1$ to $\partial\mathcal{D}_t^3$ and from $\partial\mathcal{D}_t^2$ to $\partial\mathcal{D}_t^4$.

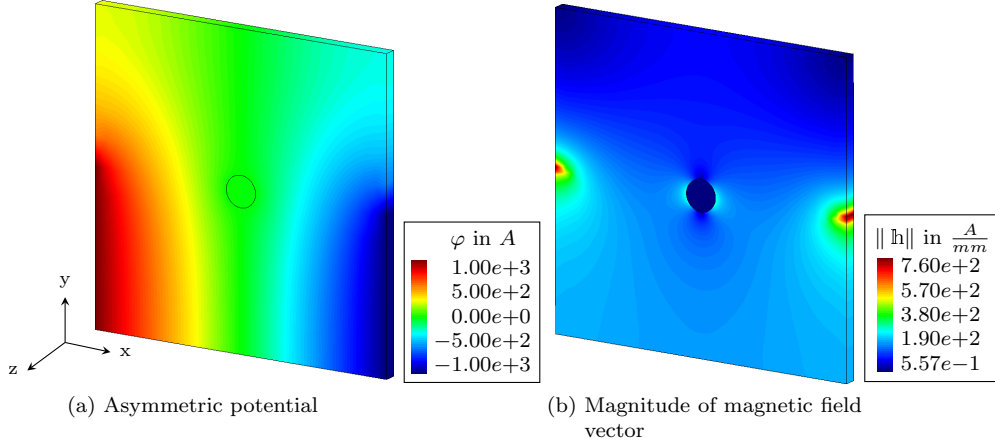


Figure 7: Single cylindrical particle (diameter 1mm) in asymmetric magnetic field generated by a scalar potential prescribed along parts of the vertical boundary

Due to the asymmetric potential field and the location of the particle, the volumetric and interface ponderomotive forces are non-symmetric overall, but do exhibit symmetry about the y-z plane. As can be inferred from fig. 8, the interface forces generate an overall upwards contribution (in the positive y direction) while the volumetric forces act downwards. Overall, the volume terms dominate and the resulting force, and therefore the displacement in the non-rigid case, is in the negative y direction.

In the forthcoming examples, we study the influence of grid refinement, size and offset as well as shape of the particle on the resultant ponderomotive force and torque. The outer dimensions of the computational domain \mathcal{D}_t , edge length l and thickness t , remain unchanged as in section 5.2. The same holds for the particle's diameter, $a = b = 1\text{mm}$, and offset $o = 0\text{mm}$ within section 5.3.1. This changes in sections 5.3.2 and 5.3.3, as we explicitly investigate the influence of the **particle's radius** and the offset when shifting the particle from the center of the computational domain to the left. In section 5.3.4 we do no longer consider a cylindrical particle, but an elliptical instead and calculate the resultant ponderomotive force and torque for varying inclinations of the ellipse.

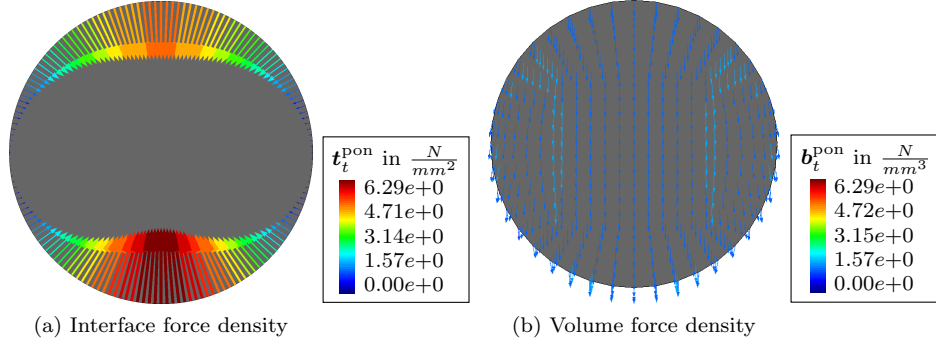


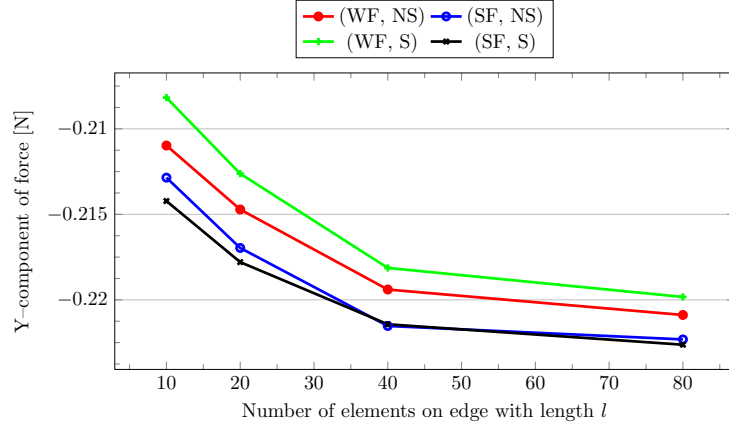
Figure 8: Nodal representation of ponderomotive force densities computed by the smooth version of strong force implementation (SF, S) in the magnetized particle (diameter 1mm) centered in an asymmetric magnetic field

5.3.1. Effect of grid refinement

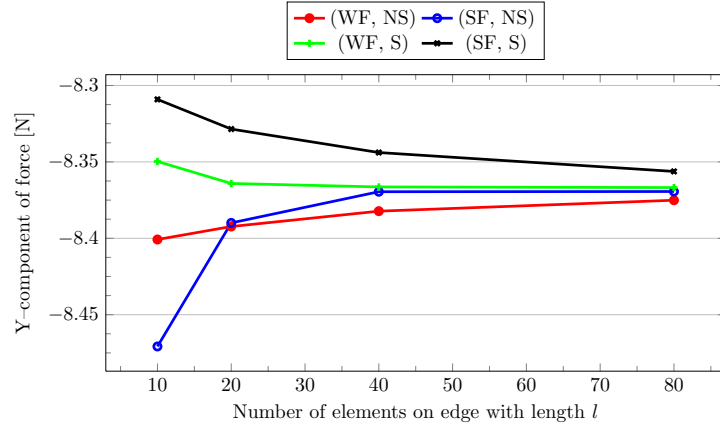
To assess the effect of grid refinement on the accuracy of the force computation, we determine the total ponderomotive force by the strong and the weak technique and compare both results for different refinements. The result of the convergence study is shown in fig. 9a for the particle \mathcal{B}_t^2 and in fig. 9b for the entire computational domain \mathcal{D}_t . The outer edge with length l was the primary focus of refinement, but additional refinement in other areas of the domain was performed to maintain a largely consistent aspect ratio of the elements.

The results demonstrate that all calculation approaches tend to converge to a common value for the force generated within the particle and the entire domain. Focusing on the particle, the method derived from the weak formulation predicts a lower force than that from the strong formulation. The use of smoothed or non-smoothed magnetic quantities is almost negligible for the strong form computation, while it is significant in the weak case. In terms of computing the resultant force on the entire domain, the weak approach produces more consistent results as the deviation from the limit value is already small for the coarsest mesh. Non-smooth quantities underestimate the resultant domain force in comparison to the computation with smoothed quantities. When comparing the force values in fig. 9a in contrast to those in fig. 9b, a supplementary observation is that the total force generated in the matrix is far greater than that in the particle. This can be attributed to the volume difference between the particle and the surrounding medium.

Overall, the difference in results between the two methods of magnetic force computation is minor. The one derived from the virtual work equation is easy to implement and, relative to the strong method, quick to compute. However, the second procedure derived directly from the strong form of the governing equations provides insights with greater detail as we can easily distinguish between forces acting on the material interface and those generated inside the volume. Furthermore, it is possible to compute the



(a) Particle



(b) Entire domain

Figure 9: Computed y-component of ponderomotive force generated within the particle (diameter 1mm) and the entire domain for increasing number of elements on edge with length l

ponderomotive torque using the second approach. Therefore, from this point on, we will focus on the latter framework in conjunction with the smoothing of the magnetic quantities prior to post-processing.

5.3.2. Size effect

With the center of the particle remaining in the center of the domain, we reduce the diameter of the particle and observe a considerable difference in the magnetic

effects. Illustrated in fig. 10 is the magnetic field in the particle and a diagrammatic representation of the resulting ponderomotive force. As the particle is decreased in size, the magnetic field that permeates the particle becomes more uniform and the generated force declines.

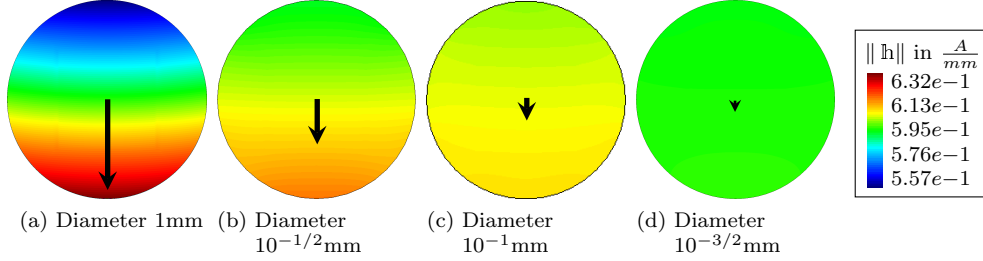


Figure 10: Magnetic field and ponderomotive resultant force ((SF, S) computation) developed within the magnetized particle with varying diameter in an asymmetric field. The force vector are not to scale.

When comparing the tractions along the interface of the smallest particle in fig. 11 with those of the largest particle in fig. 8, the uniformity of the internal and external field in the smaller case results in a reduction of the resultant interface force. However, both the volume and surface force densities developed in the smaller particle remain of similar magnitude to that of the larger one. Nevertheless, the resulting forces are smaller due to the difference in surface area and volume.

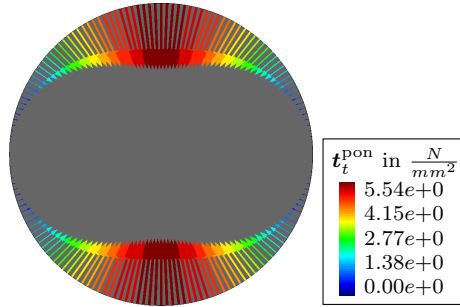


Figure 11: Nodal representation of ponderomotive interface force density ((SF, S) computation) produced in the smallest magnetized particle (diameter $10^{-3/2}$ mm) centered in an asymmetric field.

Depicted in fig. 12 is the relationship between the particle size and the induced ponderomotive force. The exponent of the force magnitude decreases proportionally to the exponent of the particle diameter. The relationship is due to the effective homogenization of the internal magnetic field, as well as the 2.5d nature of the geometry. In all cases, the reduction in volume force coincides with a reduction in the interface

force resulting in a constant ratio between the forces. The ratio of volume to interface force magnitudes is approximately 1.9 in each case.

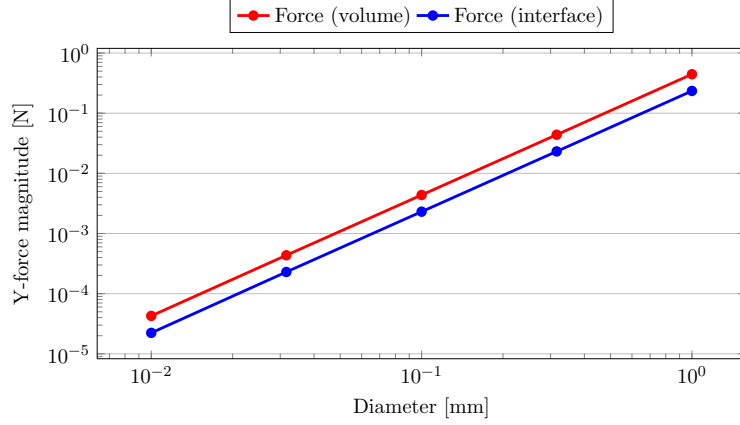


Figure 12: Interface and volume forces calculated with the strong form calculation (SF, S) in the magnetized particle with varying diameter in an asymmetric field.

5.3.3. Particle location

As the particle is moved laterally towards the source of the magnetic field, its influence on the surrounding magnetic field becomes more pronounced. Depicted in fig. 13 is the potential and magnetic field developed for a 1mm diameter particle offset by $o = 2.5\text{mm}$ in the negative x direction. When comparing fig. 13a with fig. 7b, the effect of shifting the position of the particle becomes evident. The magnetic potential within the domain is no longer symmetric and the magnetic field developed in the vicinity of the particle is non-uniform.

A substantial increase in both volume and interface forces results from the higher potential gradient in and around the particle. The force densities shown in fig. 14 indicate that the resulting forces still act to deform and translate the particle. The volumetric force is aligned with the gradient of the potential field (downwards and to the left), and dominates the resulting interface force which acts in a direction nearly orthogonal to the former. Both force density fields are completely non-homogeneous due to the non-uniformity of the potential field.

Figure 15 presents a gradated illustration of the result of shifting the rigid particle to the left. The strength of the induced magnetic field within the particle increases considerably as the particle is moved towards the boundary \mathcal{D}_t^1 . Furthermore, the average direction of the gradient of the potential field in and around the particle is rotated negatively about the z-axis. These observations collectively result in a total ponderomotive force vector that increases with the offset in magnitude and orientation towards the boundary \mathcal{D}_t^1 . The particle is attracted to the source of the potential, provided that its initial position is non-centered. It is also observed that the effective

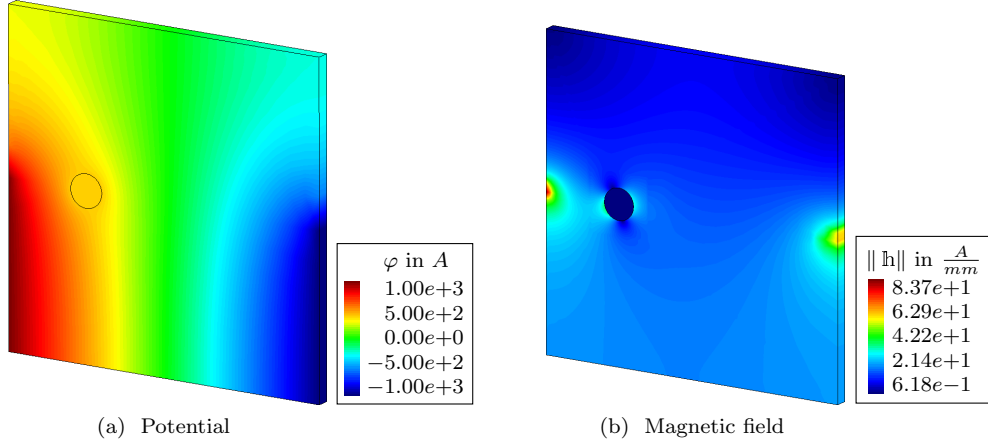


Figure 13: Cylindrical particle in asymmetric magnetic field immersed into elastomer and offset by $o = 2.5\text{mm}$ to the left side along the x-axis

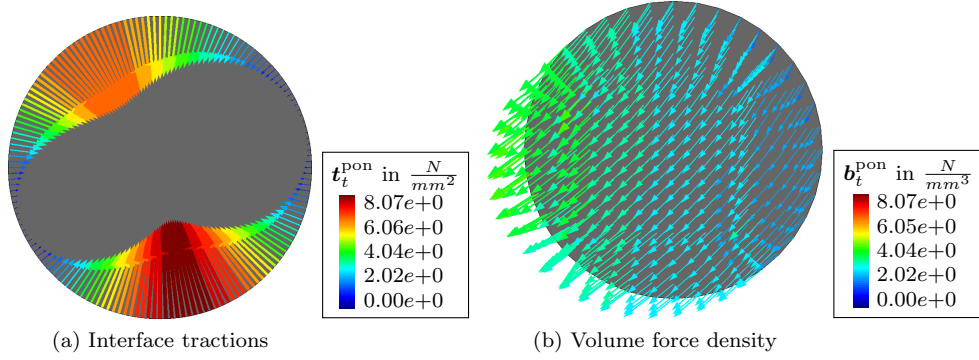


Figure 14: Nodal representation of ponderomotive interface and volume force density ((SF, S) computation) produced in the magnetized particle (diameter 1mm) offset by 2.5mm in an asymmetric field

ponderomotive moment, measured around the particle center of mass, increases as well. Thus, the particle would undergo rotation as it translates in a non-rigid situation and the degree of rotation would increase as the particle moves.

As can be seen in fig. 16, the strength of the attraction to the potential source and the out-of-plane torque of the particle increase non-linearly as the horizontal offset is increased. However, the trend is such that once the particle is closer than 2mm to the boundary on the vertical centerline of \mathcal{D}_t , the horizontal component of the magnetic force will exceed the vertical component. The magnitude of the generated torque is small due to the shape of the particle.

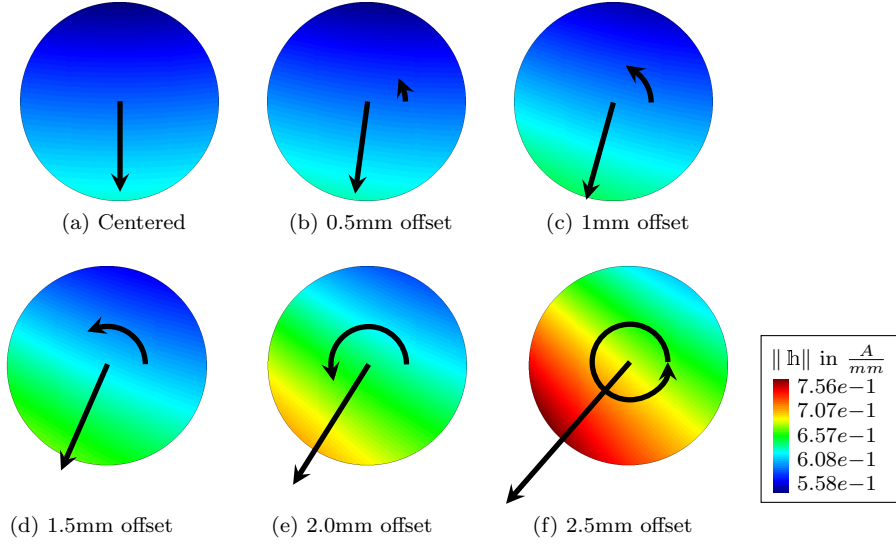


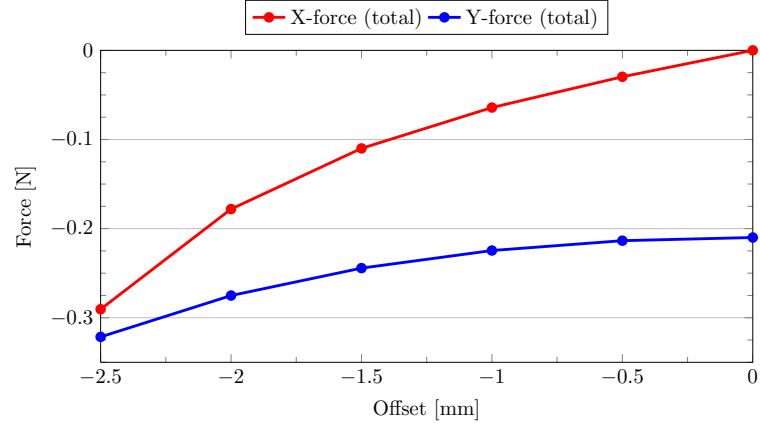
Figure 15: Magnetic field, ponderomotive resultant force and torque ((SF, S) computation) in the magnetized particle (diameter 1mm) with varying position in an asymmetric field. In this diagram, the force and torque arrows display the direction and magnitude relative to the case of maximal offset.

5.3.4. Particle shape and orientation

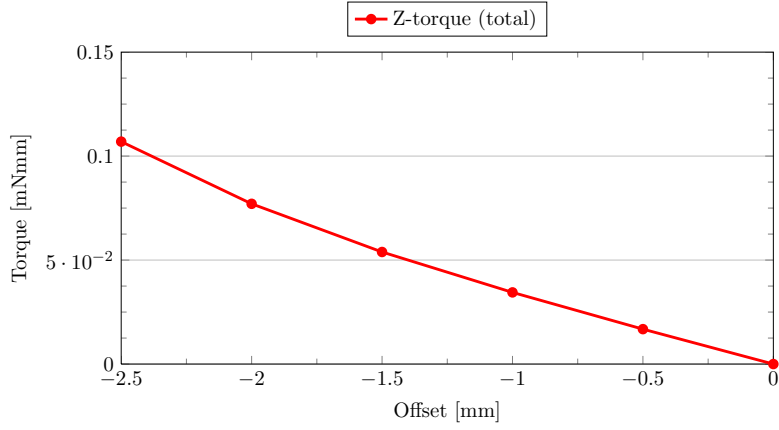
Lastly, we investigate the influence of the orientation of an elliptical particle, which is offset by $o = 1.5\text{mm}$ from the centre of \mathcal{D}_t . The particle was elongated by stretching the major axis such that $\frac{a}{b} = 2$. Changing the value of ϕ , rotates the particle in place. This rotation influences not only the alignment of the major axis of the particle with the magnetic field but also the distance of the particle-matrix interface to the intersection line $\mathcal{D}_t^1 \cap \mathcal{D}_t^3$ with high potential gradients.

Figure 17 illustrates the effect of the orientation on the ponderomotive force generated at the particle-matrix interface for an inclination of $\phi = +45$ and $\phi = -45$. Due to its disturbance of the magnetic field, large interface forces are generated when the particle is aligned with the magnetic field (fig. 17a). In both cases, there is an evident asymmetry in the traction force generated in each quadrant of the particle, which is expected to lead to the generation of a torque around the particle's centroid.

As is indicated in fig. 18a, regardless of orientation of the particle, the vertical component of the resultant ponderomotive force acts downwards. The volume and traction forces oppose each other, while the volume contribution dominates. The interplay between the x-components of the interface and volume forces is more complex in the sense that it is possible to cancel each other out. If this is not the case, then the force tends to attract the particle towards the source of potential \mathcal{D}_t^1 . The sign of the x-component of the volume and interface forces is determined by the particle's



(a) Total ponderomotive force



(b) Total ponderomotive torque

Figure 16: Interface and volume forces and magnetic torque ((SF, S) computation) produced in the magnetized particle (diameter 1mm) offset in an asymmetric field.

orientation.

Figure 18b indicates that the induced particle torque is almost completely derived from the interface contribution. The magnitude of the developed torque does not correlate with the overall magnetic force acting on the particle. The direction of the torque changes as the alignment of the major axis is changed from being parallel to perpendicular to the average magnetic field direction. Again, it is possible to orientate the particle such that no resultant torque is produced (at ϕ approximately equal to -85° and 10°). The maximal and minimal values of the torque are attained at -30°

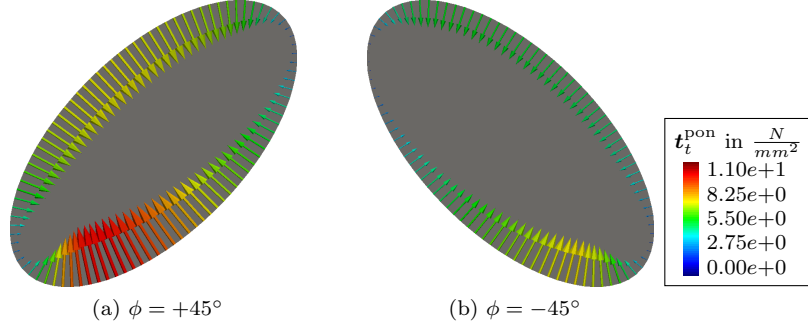


Figure 17: Nodal representation of ponderomotive interface force density ((SF, S) computation) arising from rotation of an elliptical particle offset in an asymmetric magnetic field.

and 45° respectively.

5.4. Translation of particles under the influence of a magnetic field

In our final examples, we drop the constraint on the displacement degrees of freedom and let the particle travel as the magnetic field forces it to do. Besides the magnetic material parameters, which remain as before, we assign mechanical properties of bulk modulus and shear modulus to the stiff particle ($\kappa = 121.39 \cdot 10^3 \text{MPa}$, $\mu = 59.28 \cdot 10^3 \text{MPa}$, $\mu_p = 5000$) and the very soft, non-magnetizable carrier material ($\kappa = 3.71 \text{MPa}$, $\mu = 0.38 \text{MPa}$, $\mu_m = 1$). For the moment, we assume a Neo-Hookean type material model for all composites amended by the magnetic free field energy eq. (5.1).

For the results presented in fig. 19, the geometric setup and the boundary conditions are the same as in section 5.3.1 and section 5.3.2 for a particle with the diameter of 1mm. As we have seen earlier, the resultant ponderomotive force acts downwards and thus causes the particle to travel in negative y direction towards the bottom boundary of the computational domain.

The geometric setup to generate the results in fig. 20 corresponds to section 5.3.3 with a particle offset of 15mm. However, the scalar potential is now prescribed along the whole boundary ($\mathcal{D}_t^1 \cup \mathcal{D}_t^3$ and $\mathcal{D}_t^2 \cup \mathcal{D}_t^4$) to avoid large potential gradients at the middle of the vertical boundaries. The resulting deformation tends towards the left because the particle is attracted to the boundary where the positive potential is applied.

In our final example, we consider the system in fig. 21, where two particle \mathcal{B}_t^1 and \mathcal{B}_t^3 are immersed into a carrier material \mathcal{B}_t^2 . The magnetic scalar potential is prescribed along the boundary \mathcal{D}_t^{top} and \mathcal{D}_t^{bottom} , thus generating a vertically aligned magnetic field fig. 22a. The computational domain has the dimensions $w = 9 \text{mm}$, $l = 14 \text{mm}$, $t = 0.4 \text{mm}$. The particles with a diameter of 1mm are located at (0.75, 0.75)mm and

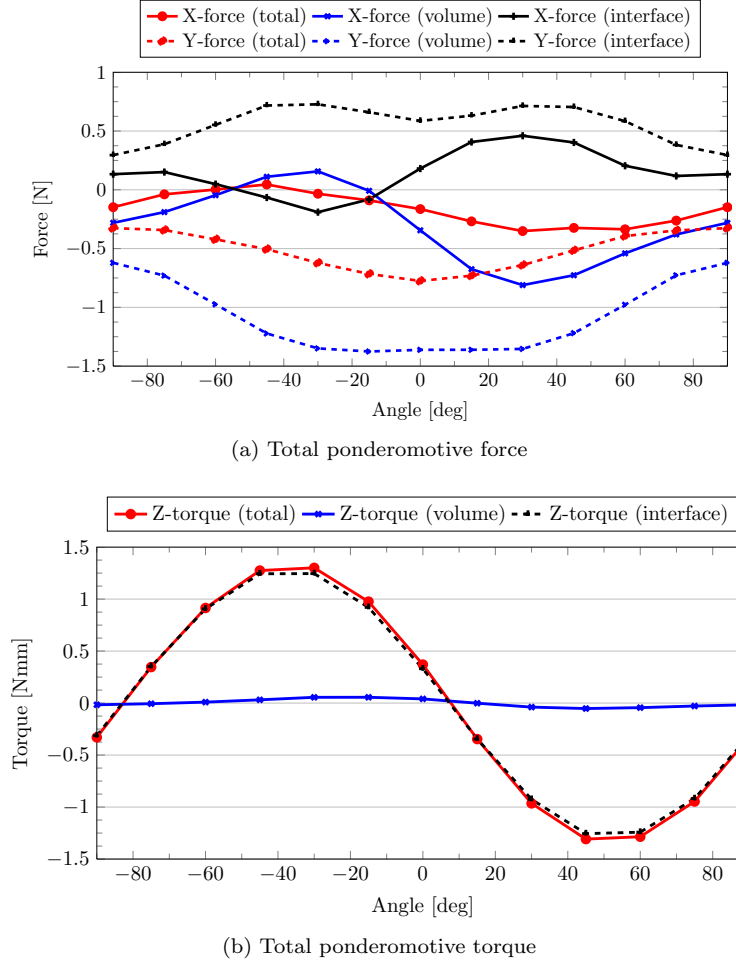


Figure 18: Interface and volume forces and magnetic torque produced in the magnetized elliptical particle offset and rotated in an asymmetric field.

$(-0.75, -0.75)$ mm. Thus, the distance between them is about $d = \frac{3\sqrt{2}}{2} \approx 2.12$ mm and the angle between the axis connecting the two and the undisturbed magnetic field is 45° . The material parameters for both particles are the same as given above. As can be observed in section 5.4, the particles rotate around each other and are attracted at the same time until they would eventually get in contact. The ponderomotive force vectors increase gradually throughout the simulation accelerating the particle more and more towards the center. The path predicted by our calculation (black solid line) bends quickly inwards taking into account the constantly increasing magnetic field. Similar results have been reported in [16] (white dashed line), where two particles are

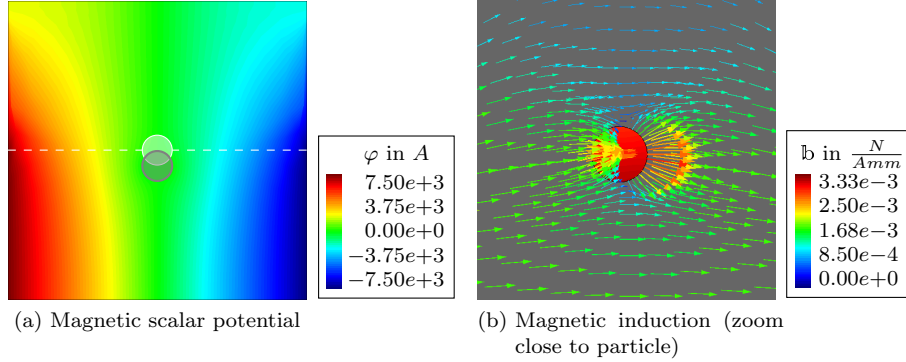


Figure 19: Magnetized particle (diameter 1mm) in an asymmetric magnetic field plotted in deformed configuration (scaled by factor 3). Translation towards the bottom boundary, evasive movement of the matrix.

immersed into in a fluid under the influence of a constant magnetic field. The deviation of the two pathways is to explain by the different applied magnetic fields and initial geometric setup.

All simulations including displacement are limited by large deformations and corresponding distortions of the mesh occurring in close proximity of the particle-matrix interface.

6. Conclusion

We have demonstrated two methods of computing localized and global ponderomotive forces and torques generated within magnetizable media. These calculations have been embedded within a finite element framework for large strain magneto-elasticity, derived from the classical descriptions of magnetostatics. The weak form of the coupled problem as based on the magnetic field as independent variable. Exploiting the constitutive law, allows a computation of the ponderomotive force and torque in terms of the magnetization and the magnetic induction, which aligns well with physics. The force and torque implementation has been verified against analytical solutions and the convergence properties of each investigated under numerous rigid scenarios. Overall, it was demonstrated that the strong form method that allows for the analysis of localized force and torque generation, restricted to individual particles, showed the most practical use and best convergence properties. The force computation derived from the weak variational form was also demonstrated to be accurate and useful in the determination of localized forces when the ratio of the relative permeabilities of the particles and carrier was large. The effect of the externally applied magnetic field on generation of interface and volume forces and torques has been presented under uniform and non-uniform fields, with particles of different size, shape and location.

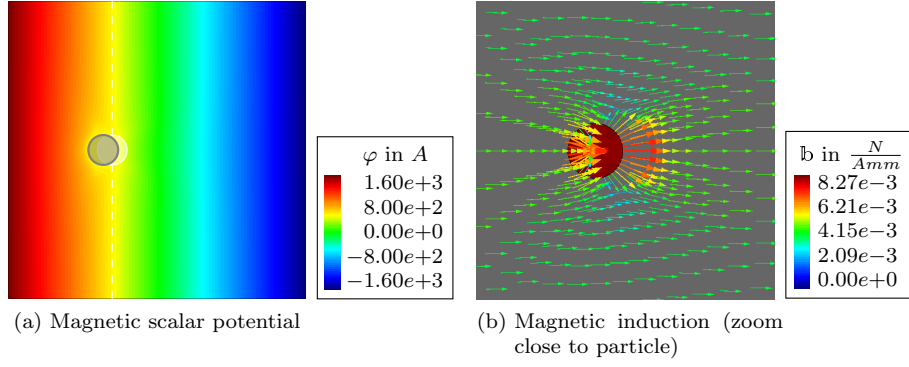


Figure 20: Magnetized particle (diameter 1mm) offset by 15mm in a symmetric magnetic field plotted in deformed configuration (scaled by factor 10). Attraction towards the boundary with positive magnetic scalar potential.

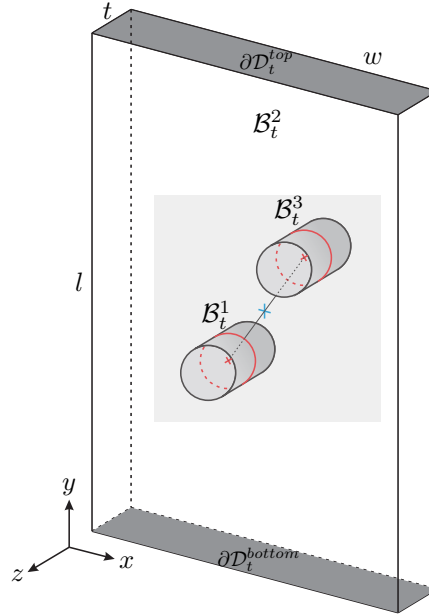


Figure 21: Diagrammatic sketch of two magnetized particles (diameter 1mm) at 45° and $3\sqrt{2}/2$ mm distance in symmetric potential.

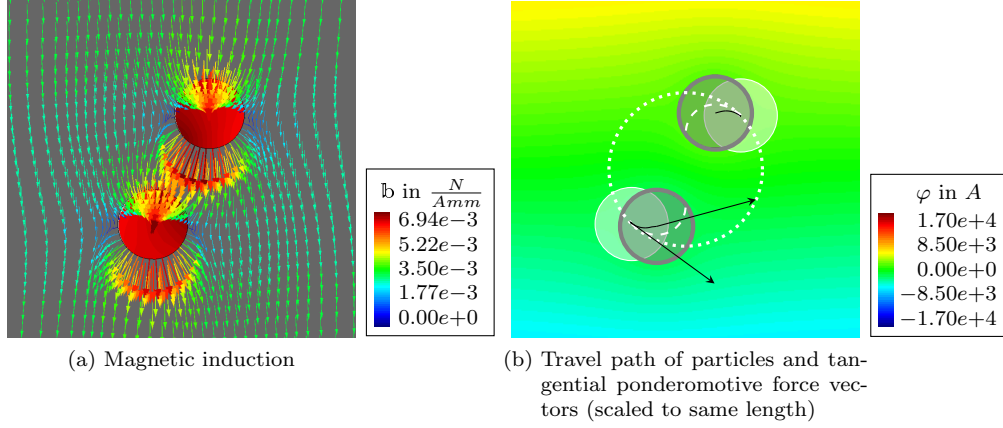


Figure 22: Two magnetized particles (diameter 1mm) at 45° and $3\sqrt{2}/2\text{mm}$ distance in symmetric potential. Rotation around common pivot at center point of computational domain.

The interplay between the bulk and surface forces has been discussed in terms of their effect on predicted particle movement and deformation.

7. Acknowledgements

The first author would like to express her gratitude to the German Research Foundation (Deutsche Forschungsgemeinschaft, DFG) for financing this work through grant STE 544/32-2. The support of this work by the European Research Council (ERC) through the Advanced Grant MOCOPOLY is gratefully acknowledged by the third and fourth authors.

A. Derivation of split representation of stresses for the Legendre transformed case

The elastic and magnetization stresses can be derived from the material constitutive law in the following manner:

$$\begin{aligned}
\frac{\partial \Psi_0^*(\mathbf{F}, \mathbb{H})}{\partial \mathbf{F}} &= \frac{\partial \Psi_0(\mathbf{F}, \mathbb{B}(\mathbb{H}))}{\partial \mathbf{F}} + \frac{\partial \Psi_0(\mathbf{F}, \mathbb{B}(\mathbb{H}))}{\partial \mathbb{B}} \cdot \frac{\partial \mathbb{B}(\mathbb{H})}{\partial \mathbf{F}} + \frac{\partial}{\partial \mathbf{F}} \left[\frac{1}{2} \mu_0 J \mathbf{C}^{-1} : [\mathbb{M} \otimes \mathbb{M}] \right] \\
&= \mathbf{P} + \mathbf{P}^{\text{mag}} + (-\mathbb{M}) \cdot \frac{\partial}{\partial \mathbf{F}} [\mu_0 J \mathbf{C}^{-1} \cdot (\mathbb{H} + \mathbb{M})] + \frac{\partial}{\partial \mathbf{F}} \left[\frac{1}{2} \mu_0 J \mathbf{C}^{-1} : [\mathbb{M} \otimes \mathbb{M}] \right] \\
&= \mathbf{P} + \mathbf{P}^{\text{mag}} - \mu_0 [\mathbb{M} \otimes \mathbb{H}] : \frac{\partial J \mathbf{C}^{-1}}{\partial \mathbf{F}} - \frac{1}{2} \mu_0 [\mathbb{M} \otimes \mathbb{M}] : \frac{\partial J \mathbf{C}^{-1}}{\partial \mathbf{F}} \\
&=: \mathbf{P} + \mathbf{P}^{*\text{mag}}.
\end{aligned}$$

Using the push-forward operation, the Piola stresses are transformed to their spatial counterparts $\boldsymbol{\sigma} = \mathbf{P} \cdot \text{cof} \mathbf{F}^{-1}$ via

$$\begin{aligned}
J^{-1} \frac{\partial \Psi_0^*(\mathbf{F}, \mathbb{H})}{\partial \mathbf{F}} \cdot \mathbf{F}^T &= \boldsymbol{\sigma} + \boldsymbol{\sigma}^{\text{mag}} - \mu_0 \left[\mathbb{m} \otimes \mathbb{h} + \frac{1}{2} \mathbb{m} \otimes \mathbb{m} \right] : [\mathbf{F} \otimes \mathbf{F}] : J^{-1} \frac{\partial J \mathbf{C}^{-1}}{\partial \mathbf{F}} \cdot \mathbf{F}^T \\
&= \boldsymbol{\sigma} + \boldsymbol{\sigma}^{\text{mag}} - (\mathbb{m} \cdot \mathbb{b}) \mathbf{i} + \mathbb{m} \otimes \mathbb{b} + \mu_0 \mathbb{h} \otimes \mathbb{m} + \mu_0 \frac{1}{2} (\mathbb{m} \cdot \mathbb{m}) \mathbf{i} \\
&= \boldsymbol{\sigma} + \mu_0 \mathbb{h} \otimes \mathbb{m} + \mu_0 \frac{1}{2} (\mathbb{m} \cdot \mathbb{m}) \mathbf{i} \\
&=: \boldsymbol{\sigma} + \boldsymbol{\sigma}^{*\text{mag}}.
\end{aligned}$$

B. Derivation of boundary formulation for magnetic force computation

Noting the domain decomposition shown in fig. 2, the virtual work performed by the ponderomotive force defined in eq. (2.21) acting on the computational domain \mathcal{D}_t is

$$\delta W^{\text{pon}} := \int_{\mathcal{D}_t} \delta \varphi \cdot \mathbf{b}_t^{\text{pon}} + \int_{\partial \mathcal{B}_t^2} \delta \varphi \cdot \mathbf{t}_t^{\text{pon}}, \quad (\text{B.1})$$

where $\delta\varphi$ is the virtual displacement. Application of eq. (2.11)₁ and the divergence theorem to the volume integral leads to

$$\begin{aligned}
& \int_{\mathcal{D}_t} \delta\varphi \cdot \mathbf{b}_t^{\text{pon}} \\
&= \int_{\partial\mathcal{B}_t^2} \delta\varphi \cdot [\boldsymbol{\sigma}^{\text{pon}} \cdot \mathbf{n}_2^+] - \int_{\mathcal{B}_t^2} \nabla_{\mathbf{x}} \delta\varphi : \boldsymbol{\sigma}^{\text{pon}} \quad (\text{particle}) \quad (\text{B.2}) \\
&+ \int_{\partial\mathcal{B}_t^2} \delta\varphi \cdot [\boldsymbol{\sigma}^{\text{pon}} \cdot \mathbf{n}_2^-] + \int_{\partial\mathcal{D}_t} \delta\varphi \cdot [\boldsymbol{\sigma}^{\text{pon}} \cdot \mathbf{n}_{\partial\mathcal{D}_t}^+] - \int_{\mathcal{B}_t^1} \nabla_{\mathbf{x}} \delta\varphi : \boldsymbol{\sigma}^{\text{pon}} \quad (\text{matrix})
\end{aligned}$$

Using eq. (2.20) to collect terms pertaining to internal material interfaces results in the domain virtual work

$$\delta W^{\text{pon}} = \int_{\partial\mathcal{D}_t} \delta\varphi \cdot [\boldsymbol{\sigma}^{\text{pon}} \cdot \mathbf{n}_{\partial\mathcal{D}_t}^+] - \int_{\mathcal{D}_t} \nabla_{\mathbf{x}} \delta\varphi : \boldsymbol{\sigma}^{\text{pon}} = \sum_I \delta\varphi_I \cdot \mathbf{f}_I^{\text{pon}}. \quad (\text{B.3})$$

References

- [1] B. Avci and P. Wriggers. A DEM-FEM Coupling Approach for the Direct Numerical Simulation of 3D Particulate Flows. *Journal of Applied Mechanics*, 79(1):010901, 2012.
- [2] A. Boczkowska, L. Czechowski, M. Jaroniek, and T. Niezgoda. Analysis of magnetic field effect on ferromagnetic spheres embedded in elastomer pattern. *Journal of Theoretical and Applied Mechanics*, 48(3):659–676, 2010.
- [3] H. Böse, R. Rabindranath, and J. Ehrlich. Soft magnetorheological elastomers as new actuators for valves. *Journal of Intelligent Material Systems and Structures*, 23(9):989–994, 2012.
- [4] W. F. Brown. *Magnetoelastic interactions*. Springer, Berlin and Heidelberg and New York, 1966.
- [5] R. Bustamante, A. Dorfmann, and R. W. Ogden. Universal relations in isotropic nonlinear magnetoelasticity. *Quarterly Journal of Mechanics and Applied Mathematics*, 59(3):435–450, 2006.
- [6] A. DeSimone and P. Podio-Guidugli. On the continuum theory of deformable ferromagnetic solids. *Archive for Rational Mechanics and Analysis*, 136:201–233, 1996. ISSN 0003-9527.
- [7] A. Dorfmann and R.W Ogden. Nonlinear magnetoelastic deformations of elastomers. *Acta Mechanica*, 167(1-2):13–28, 2003.

- [8] A. Dorfmann and R.W Ogden. Nonlinear magnetoelastic deformations. *Quarterly Journal of Mechanics and Applied Mathematics*, 57(4):599–622, 2004.
- [9] F. Durst. *Grundlagen der Strömungsmechanik: Eine Einführung in die Theorie der Strömung von Fluiden*. Springer-Verlag, Berlin and Heidelberg, 2006.
- [10] A.C Eringen. *Mechanics of continua*. Robert E. Krieger Publishing Company, Huntington, NY, 1980.
- [11] A.C Eringen and G.A Maugin. *Electrodynamics of Continua*. Springer, Berlin, 1990.
- [12] M. Farshad and A. Benine. Magnetoactive elastomer composites. *Polymer Testing*, 23(3):347–353, 2004.
- [13] E. Galipeau and P. Ponte Castañeda. A finite-strain constitutive model for magnetorheological elastomers: Magnetic torques and fiber rotations. *Journal of the Mechanics and Physics of Solids*, 61(4):1065–1090, 2013.
- [14] D.J Griffiths. *Introduction to electrodynamics*. Prentice-Hill, Inc, Englewood Cliffs and New Jersey, 1989.
- [15] K. Han, Y.T Feng, and D.R.J Owen. Three-dimensional modelling and simulation of magnetorheological fluids. *International Journal for Numerical Methods in Engineering*, 84(11):1273–1302, 2010.
- [16] T. Kang, M. Hulsen, J. Dentoonder, P. Anderson, and H. Meijer. A direct simulation method for flows with suspended paramagnetic particles. *Journal of Computational Physics*, 227(9):4441–4458, 2008.
- [17] S.V Kankanala and N. Triantafyllidis. On finitely strained magnetorheological elastomers. *Journal of the Mechanics and Physics of Solids*, 52(12):2869–2908, 2004.
- [18] E. Keaveny and M. Maxey. Modeling the magnetic interactions between paramagnetic beads in magnetorheological fluids. *Journal of Computational Physics*, 227(22):9554–9571, 2008.
- [19] H. Kitahara, H. Kotera, and S. Shima. 3-D simulation of magnetic particles’ behaviour during compaction in a magnetic field. *Powder Technology*, 109(1-3): 234–240, 2000.
- [20] D.J Klingenberg. Magnetorheology: applications and challenges. *AIChE Journal*, 47(2):246–249, 2001.
- [21] A. Kovetz. *Electromagnetic theory*. Oxford University Press, Oxford and New York, 2000.

- [22] H.V Ly, F. Reitich, M.R Jolly, H.T Banks, and K. Ito. Simulations of Particle Dynamics in Magnetorheological Fluids. *Journal of Computational Physics*, 155: 160–177, 1999.
- [23] G.A Maugin. Deformable Magnetically Saturated Media. I. Field Equations. *Journal of Mathematical Physics*, 13(2):143, 1972.
- [24] G.A Maugin. A continuum theory of deformable ferrimagnetic bodies. I. Field equations. *Journal of Mathematical Physics*, 17(9):1727–1738, 1975.
- [25] G.A Maugin. *Continuum mechanics of electromagnetic solids*. North-Holland, 1988. ISBN 0444703993.
- [26] G.A Maugin. On modelling electromagnetomechanical interactions in deformable solids. *International Journal of Advances in Engineering Sciences and Applied Mathematics*, 1(1):25–32, 2009.
- [27] V.Q Nguyen, A.S Ahmed, and R.V Ramanujan. Morphing soft magnetic composites. *Advanced Materials*, 24(30):4041–4054, 2012.
- [28] Y.H Pao. Electromagnetic forces in deformable continua. In S. Nemat-Nasser, editor, *Mechanics today*. Pergamon Press, New York, 1978.
- [29] P. Ponte Castañeda and E. Galipeau. Homogenization-based constitutive models for magnetorheological elastomers at finite strain. *Journal of the Mechanics and Physics of Solids*, 59(2):194–215, 2011.
- [30] E. Rank and O.C Zienkiewicz. A simple error estimator in the finite element method. *Communications in Applied Numerical Methods*, 3(3):243–249, 1987.
- [31] J. Ravník and M. Hriberšek. High gradient magnetic particle separation in viscous flows by 3D BEM. *Computational Mechanics*, 51(4):465–474, 2013.
- [32] S. Sassi, K. Cherif, L. Mezghani, M. Thomas, and A. Kotrane. An innovative magnetorheological damper for automotive suspension: from design to experimental characterization. *Smart Materials and Structures*, 14(4):811, 2005.
- [33] J. C. Simo and J. E. Marsden. On the rotated stress tensor and the material version of the Doyle-Ericksen formula. *Archive for Rational Mechanics and Analysis*, 86(3):213–231, 1984.
- [34] D. J. Steigmann. Equilibrium theory for magnetic elastomers and magnetoelastic membranes. *International Journal of Non-Linear Mechanics*, 39(7):1193–1216, 2004.
- [35] P. Steinmann. Computational nonlinear electro-elasticity – getting started: Mechanics and Electrodynamics of Magneto- and Electro-elastic Materials. In R.W Ogden and D.J Steigmann, editors, *Mechanics and Electrodynamics of Magneto- and Electro-elastic Materials*, volume 527 of *CISM Courses and Lectures*. Springer, Vienna, 2011.

- [36] J.A Stratton. *Electromagnetic theory*. International series in pure and applied physics. McGraw-Hill, New York, 1941.
- [37] H. F. Tiersten. Coupled magnetomechanical equations for magnetically saturated insulators. *Journal of Mathematical Physics*, 5(9):1298–1318, 1964.
- [38] R.A Toupin. The elastic dielectric. *Journal of Rational Mechancis and Analysis*, 5:849–915, 1956.
- [39] J. de Vicente, G. Bossis, S. Lacis, and M. Guyot. Permeability measurements in cobalt ferrite and carbonyl iron powders and suspensions. *Journal of Magnetism and Magnetic Materials*, 251(1):100–108, 2002.
- [40] F. Vogel, R. Bustamante, and P. Steinmann. On some mixed variational principles in electro-elastostatics. *International Journal of Non-Linear Mechanics*, 47(2): 341–354, 2012.
- [41] F. Vogel, R. Bustamante, and P. Steinmann. On some mixed variational principles in magneto-elastostatics. *International Journal of Non-Linear Mechanics*, 51:157–169, 2013.
- [42] D.K Vu and P. Steinmann. Nonlinear electro- and magneto-elastostatics: Material and spatial settings. *International Journal of Solids and Structures*, 44(24):7891–7905, 2007.
- [43] D.K Vu, P. Steinmann, and G. Possart. Numerical Modelling of the Non-Linear Electroelasticity. *International Journal for Numerical Methods in Engineering*, 70(6):685–704, 2007.
- [44] H. Yin, L. Sun, and J. Chen. Magneto-elastic modeling of composites containing chain-structured magnetostrictive particles. *Journal of the Mechanics and Physics of Solids*, 54(5):975–1003, 2006.
- [45] O.C Zienkiewicz and J.Z Zhu. A simple error estimator and adaptive procedure for practical engineering analysis. *International Journal for Numerical Methods in Engineering*, 24(2):337–357, 1987.